



Publication Year	2020
Acceptance in OA	2022-03-17T10:24:12Z
Title	The TOI-763 system: sub-Neptunes orbiting a Sun-like star
Authors	Fridlund, M., Livingston, J., Gandolfi, D., Persson, C. M., Lam, K. W. F., Stassun, K. G., Hellier, C., Korth, J., Hatzes, A. P., Malavolta, L., Luque, R., Redfield, S., Guenther, E. W., Albrecht, S., Barragan, O., BENATTI, SERENA, Bouma, L., Cabrera, J., Cochran, W. D., Csizmadia, S., Dai, F., Deeg, H. J., Esposito, M., Georgieva, I., Grziwa, S., González Cuesta, L., Hirano, T., Jenkins, J. M., Kabath, P., Knudstrup, E., Latham, D. W., Mathur, S., Mullally, S. E., Narita, N., Nowak, G., Olofsson, A. O. H., Palle, E., Pätzold, M., Pompei, E., Rauer, H., Ricker, G., Rodler, F., Seager, S., Serrano, L. M., Smith, A. M. S., Spina, L., Subjak, J., Tenenbaum, P., Ting, E. B., Vanderburg, A., Vanderspek, R., Van Eylen, V., Villanueva, S., Winn, J. N.
Publisher's version (DOI)	10.1093/mnras/staa2502
Handle	http://hdl.handle.net/20.500.12386/31644
Journal	MONTHLY NOTICES OF THE ROYAL ASTRONOMICAL SOCIETY
Volume	498



The TOI-763 system: sub-Neptunes orbiting a Sun-like star

M. Fridlund^{1,2,★}, J. Livingston³, D. Gandolfi⁴, C. M. Persson², K. W. F. Lam⁵, K. G. Stassun⁶, C. Hellier⁷, J. Korth⁸, A. P. Hatzes⁹, L. Malavolta¹⁰, R. Luque^{11,12}, S. Redfield¹³, E. W. Guenther⁹, S. Albrecht¹⁴, O. Barragan¹⁵, S. Benatti¹⁶, L. Bouma¹⁷, J. Cabrera¹⁸, W. D. Cochran^{19,20}, S. Csizmadia¹⁸, F. Dai^{17,21}, H. J. Deeg^{11,12}, M. Esposito⁹, I. Georgieva², S. Grziwa⁸, L. González Cuesta^{11,12}, T. Hirano²², J. M. Jenkins²³, P. Kabath²⁴, E. Knudstrup¹⁴, D. W. Latham²⁵, S. Mathur^{11,12}, S. E. Mullally²⁶, N. Narita^{11,27,28,29,30}, G. Nowak^{11,12}, A. O. H. Olofsson², E. Palte^{11,12}, M. Pätzold⁸, E. Pompei³¹, H. Rauer^{5,18,32}, G. Ricker²¹, F. Rodler³¹, S. Seager^{21,26,33}, L. M. Serrano⁴, A. M. S. Smith¹⁸, L. Spina^{34,35}, J. Subjak^{24,36}, P. Tenenbaum³⁷, E. B. Ting²³, A. Vanderburg³⁸, R. Vanderspek²¹, V. Van Eylen³⁹, S. Villanueva²¹ and J. N. Winn¹⁷

Affiliations are listed at the end of the paper

Accepted 2020 August 14. Received 2020 August 11; in original form 2020 July 6

ABSTRACT

We report the discovery of a planetary system orbiting TOI-763(aka CD-39 7945), a $V = 10.2$, high proper motion G-type dwarf star that was photometrically monitored by the *TESS* space mission in Sector 10. We obtain and model the stellar spectrum and find an object slightly smaller than the Sun, and somewhat older, but with a similar metallicity. Two planet candidates were found in the light curve to be transiting the star. Combining *TESS* transit photometry with HARPS high-precision radial velocity (RV) follow-up measurements confirm the planetary nature of these transit signals. We determine masses, radii, and bulk densities of these two planets. A third planet candidate was discovered serendipitously in the RV data. The inner transiting planet, TOI-763 b, has an orbital period of $P_b = 5.6$ d, a mass of $M_b = 9.8 \pm 0.8 M_\oplus$, and a radius of $R_b = 2.37 \pm 0.10 R_\oplus$. The second transiting planet, TOI-763 c, has an orbital period of $P_c = 12.3$ d, a mass of $M_c = 9.3 \pm 1.0 M_\oplus$, and a radius of $R_c = 2.87 \pm 0.11 R_\oplus$. We find the outermost planet candidate to orbit the star with a period of ~ 48 d. If confirmed as a planet, it would have a minimum mass of $M_d = 9.5 \pm 1.6 M_\oplus$. We investigated the *TESS* light curve in order to search for a mono transit by planet d without success. We discuss the importance and implications of this planetary system in terms of the geometrical arrangements of planets orbiting G-type stars.

Key words: planets and satellites: detection – planets and satellites: individual: TOI-763 – planets and satellites: individual: TIC 178819686.

1 INTRODUCTION

Understanding our origin is a strong driver for science. In astrophysics and space sciences, research in exoplanets and of the Solar system is one way to gain knowledge about our place in the Universe and eventually provide a context for the existence of life on Earth. With the discovery of the first exoplanet in 1995 (Mayor & Queloz 1995) and the subsequent detection of what is now (2020 July) 4171 confirmed exoplanets,¹ the expansion of this field has led to new and fantastic discoveries that have changed the pre-1995 predictions of what planetary systems look like.

In the last ~ 15 yr, a number of space missions, namely *CoRoT* (Baglin 2003; Baglin & CoRoT Team 2016), *Kepler* (Borucki et al. 2010), *K2* (Howell et al. 2014), and *TESS* (Ricker et al. 2015),

have been launched with the objective of discovering transiting exoplanets and to derive planetary parameters with high precision. Together with the physical parameters of the exoplanets, the architecture of the systems (defined as the distribution of different categories of planets within their individual systems) has been of extraordinary interest. Thus, one of the most important findings in exoplanetology, so far, is the enormous diversity in the types of planetary systems. While not understood so far, this diversity must reflect the conditions of formation of the systems. In this context, the host star being the dominating body in each system is very important. Among different stellar types, it is especially interesting to study the planetary architectures of G-type host stars since the only known habitable planet, our Earth, orbits such a star.

There are relatively few planets smaller than Neptune for which both the size and mass has been measured. Only 70 such planets are reported orbiting G stars in the NASA archive as of 2020 June. Most of these have large uncertainties leading to errors in density

* E-mail: malcolm.fridlund@chalmers.se

¹ <https://exoplanetarchive.ipac.caltech.edu>.

Table 1. Main identifiers, equatorial coordinates, proper motion, parallax, optical and infrared magnitudes, and fundamental parameters of TOI-763.

Parameter	Value	Source
Main identifiers		
TIC	178819686	ExoFOP
CD-39 7945		CD
2MASS	J12575245–3945275	ExoFOP
UCAC4	252–056134	ExoFOP
WISE	J125752.37–394528.5	ExoFOP
APASS	18487092	ExoFOP
Gaia DR2	6140553127216043648	Simbad
Equatorial coordinates, parallax, and proper motion		
RA (J2000.0)	12 ^h 57 ^m 52 ^s .45	Gaia DR2
Dec. (J2000.0)	–39°45′27″.71	Gaia DR2
π (mas)	10.4837 ± 0.0495	Gaia DR2
μ_α (mas yr ^{–1})	–76.902 ± 0.073	Gaia DR2
μ_δ (mas yr ^{–1})	–84.817 ± 0.055	Gaia DR2
Optical and near-infrared photometry		
TESS	9.528 ± 0.006	TIC v8
G	9.9992 ± 0.0002	Gaia DR2
B _p	10.3832 ± 0.0005	Gaia DR2
R _p	9.4791 ± 0.0012	Gaia DR2
B	10.855 ± 0.028	APASS
V	10.156 ± 0.041	APASS
g	10.464 ± 0.034	APASS
J	8.858 ± 0.029	2MASS
H	8.554 ± 0.023	2MASS
K _s	8.490 ± 0.021	2MASS
W1	8.422 ± 0.023	AllWISE
W2	8.476 ± 0.019	AllWISE
W3	8.423 ± 0.020	AllWISE
W4	8.518 ± 0.211	AllWISE

of a factor of 2 or more. This is due to the fact that, hitherto, the exoplanetary space missions have been searching relatively faint stars where, although the diameters are known with high precision, the follow-up observations to acquire the planetary masses have usually had large errors. It is therefore important that thanks to the launch of the *TESS* mission relatively bright stars are now being searched for exoplanets. ESA’s future exoplanetary mission *PLATO* (Rauer et al. 2014) will have planets orbiting G stars as a primary objective when it launches in 2027.

TOI-763 is a relatively bright G-type star (Table 1). The detection by *TESS* of the possible transit of two mini-Neptune planets with radii of 2–3 R_\oplus , and having orbital periods of 5.6 and 12.3 d, respectively, is therefore of significant interest and motivates our detailed study. During the follow-up of TOI-763b and c, deriving masses of 9.8 and 9.3 M_\oplus , respectively, we found serendipitously, in the radial velocity (RV) data, a signature that could be caused by a third planet of similar mass and orbiting the host star every ~ 48 d. Together with a number of recently published systems studied by the *TESS* mission (e.g. Díaz et al. 2020; Nielsen et al. 2020), TOI-763 thus belongs to a still small but growing group of G-type stars hosting a compact planet system. Such a configuration is in sharp contrast to our own Solar system, but appears to be quite common among the exoplanetary systems discovered to date (Marcy et al. 2014). Studies of such planetary systems promise to lead to a better understanding of their formation process.

The aim with this paper is to report the characterization of the TOI-763 planet system including investigating the possibility of a third planet. A secondary objective is to place this system into the proper

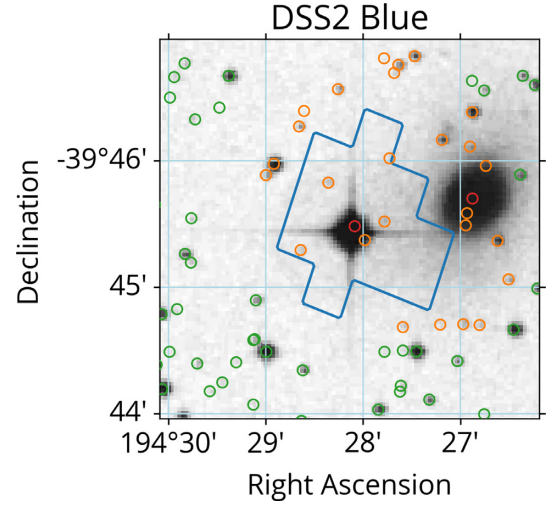


Figure 1. 3×3 arcmin² DSS2 (blue filter) image with the Sector 10 SPOC photometric aperture outlined in blue. Coloured circles denote the positions of *Gaia* DR2 sources within 2 arcmin of TOI-763; the red circle inside the aperture is TOI-763 (6140553127216043648), the red circle outside the aperture is a galaxy (6140553157278886400), the orange circles are potentially diluting sources, and other sources are in green. We establish a dilution of <1 percent for TOI-763 based on the flux contributions of all sources.

context. We present the photometry acquired by the *TESS* spacecraft in Section 2. In Section 3, we detail our follow-up work from the ground, Section 4 presents the derivation of the physical parameters of the host star. In Section 5, we describe the modelling and analysis, and derive the parameters of the planets. This is followed by the discussion in Section 6. We end the paper with our conclusions in Section 7.

2 TESS PHOTOMETRY AND TRANSIT DETECTION

TOI-763 (TIC 178819686) was observed by *TESS* in Sector 10 between 2019 March 26 and 2019 April 22 (UTC), where the target was imaged on CCD 3 of camera 2. The photometric data were sampled in the 2-min cadence mode and was processed by the Science Processing Operations Center (SPOC; Jenkins et al. 2016) data reduction pipeline. The SPOC pipeline produces time series light curve using simple aperture photometry (SAP), and the presearch data conditioning (PDCSAP) algorithm was used to remove common instrumental systematics in the light curve (Smith et al. 2012; Stumpe et al. 2012).

We investigated a 3×3 arcmin² digitized sky survey 2 (DSS-2, blue filter) image centred on TOI-763. Using the Sector 10 SPOC photometric aperture and the positions of *Gaia* Data Release 2 (DR2) sources, we established a dilution of <1 percent for TOI-763 (Fig. 1). For the light curve and transit analysis of TOI-763, we used the PDCSAP light curve publicly available in the Mikulski Archive for Space Telescopes (MAST).² The top panel of Fig. 2 shows the PDCSAP light curve of TOI-763.

Transit searches by the SPOC pipeline (Jenkins 2002) revealed the presence of two signals at 5.61 and 12.28 d in the data validation reports (Twicken et al. 2018; Li et al. 2019). The detections were

²<https://archive.stsci.edu/tess/>.

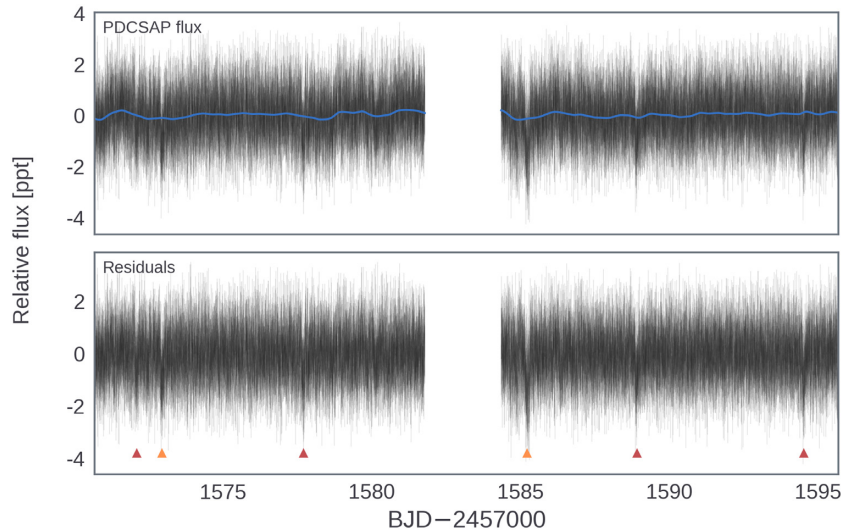


Figure 2. Upper panel: *TESS* Sector 10 PDCSAP light curve with GP model overplotted in blue. Lower panel: the ‘flattened’ light curve resulting from removing the GP model; the red and orange triangles indicate the transits of planets b and c, respectively.

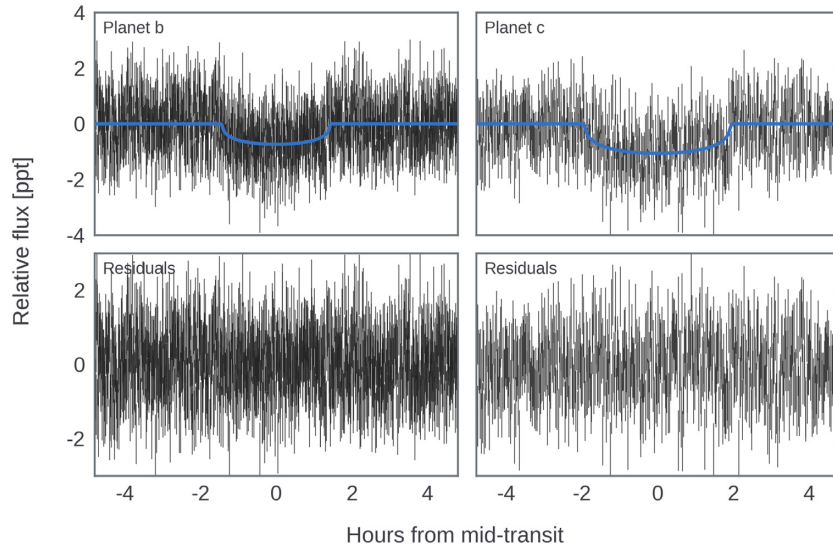


Figure 3. Flattened *TESS* photometry (black) folded on the best-fitting orbital periods of the two transiting planets, with transit models overplotted in blue (Section 5).

announced as planetary candidates via the TOI releases portal.³ We iteratively searched the PDCSAP light curve for transit signals using the Détection Spécialisée de Transits (DST) algorithm (Cabrera et al. 2012). The algorithm first applies the Savitzky–Golay method (Savitzky & Golay 1964; Press et al. 2002) to filter variability in the light curve, then uses a parabolic transit model for transit searches. A 12.27 ± 0.01 d transit signal was first detected, which has a transit depth of 813 ± 67 ppm and a duration of 4.07 ± 0.18 h. After filtering the 12.27-d signal, a second transit signal at 5.60 d was detected where transits have a depth of 620 ± 54 ppm and a transit duration of 2.66 ± 0.13 h. Our detection algorithm recovered the transit signals of both TOIs and no further significant periodic transit signal was detected (Fig. 3).

Shallow transits that are close to the noise limit of the light curve may be filtered out by the detection algorithms. We incrementally

varied the window size of the Savitzky–Golay filter and visually inspected the light curve of TOI-763 in order to search for further single transit events. No significant events were found. The transit least-squares algorithm (TLS; Hippke & Heller 2019) was also implemented to search for single, shallow transit events by fixing the maximum trial period to the observed time baseline of *TESS* Sector 10. This independently confirmed that no single transit event is found above the noise level of the light curve.

3 GROUND-BASED FOLLOW-UP OBSERVATIONS

3.1 HARPS RV observations

We acquired 74 high-resolution ($R \approx 115\,000$) spectra of TOI-763 using the HARPS fibre-fed Echelle spectrograph (Mayor et al. 2003) mounted at the ESO 3.6-m telescope of La Silla observatory (Chile). The observations were performed between 2019 June 21 and

³<https://tess.mit.edu/toi-releases/>.

September 1 (UTC), as part of our HARPS follow-up program of *TESS* transiting planets (program ID: 1102.C-0923; PI: D. Gandolfi). We used the second fibre of the spectrograph to monitor the sky-background and set the exposure time to 1500–2400 s, depending on sky conditions and schedule constraints. We reduced the HARPS data using the dedicated data reduction software (*drfs*) and extracted the RV measurements by cross-correlating the extracted Echelle spectra with a G2 numerical mask (Baranne et al. 1996; Pepe et al. 2002; Lovis & Pepe 2007). Following the method described in Malavolta et al. (2017), we corrected 27 HARPS measurements for scattered moonlight contamination. We also used the *drfs* to extract the Ca II H & K lines activity indicator ($\log R'_{\text{HK}}$), and three profile diagnostics of the cross-correlation function (CCF), namely the contrast, the full width at half-maximum (FWHM), and the bisector inverse slope (BIS). We finally used the spectrum RV analyser (*serval*; Zechmeister et al. 2018) to extract four additional activity diagnostics, namely, the chromatic RV index (Crx), differential line width (dLW), and the Na D and H α line indexes.

The *drfs* HARPS RV measurements and their uncertainties, alongside the Barycentric Julian Date in barycentric dynamical time (BJD_{TDB}), the exposure time (T_{exp}), the signal-to-noise ratio (S/N) per pixel at 5500 Å, and the eight activity diagnostics (BIS, FWHM, contrast, dLW, Crx, Na D, H α , and $\log R'_{\text{HK}}$) are listed in Tables A1 and A2.

3.2 Frequency analysis of the HARPS measurements

We performed a frequency analysis of the *drfs* RV measurements and *drfs/serval* activity indicators to look for the Doppler reflex motion induced by the two planets transiting TOI-763 and unveil the presence of potential additional signals in the time series.

The generalized Lomb–Scargle (GLS) periodogram (Zechmeister & Kürster 2009) of the HARPS measurements (Fig. 4, upper panel) shows a significant peak at the orbital frequency of TOI-763 b ($f_b = 0.178 \text{ d}^{-1}$). We derived its false alarm probability (FAP) following the bootstrap randomization method described in Murdoch, Hearnshaw & Clark (1993). Briefly, we created 10^6 random shuffles of the RV data, while keeping the time stamps fixed, and found that over the frequency range 0–0.50 d^{-1} , there were only 14 instances where ‘random’ data had power in the periodogram greater than the peak seen at f_b . The FAP is thus $14/10^6 = 1.4 \times 10^{-5}$.

The GLS periodogram of the HARPS RV residuals (Fig. 4, second panel) – following the subtraction of the Doppler signal induced by the inner planet – displays a significant peak almost at the orbital frequency of TOI-763 c ($f_c = 0.081 \text{ d}^{-1}$). We applied the same procedure to estimate its FAP and found that none of the periodograms computed from the 10^6 random shuffles of the RV residuals has a power greater than the peak at f_c . The FAP is thus $< 10^{-6}$ over the frequency range 0–0.50 d^{-1} .

The two Doppler signals at f_b and f_c have no counterpart in the periodograms of the eight activity indicators (Fig. 4), confirming the planetary nature of the two transit signals detected in the *TESS* light curve.

Following the subtraction of the Doppler reflex motion induced by the two transiting planets, the periodogram of the HARPS RV residuals shows an additional peak at about 48 d (0.021 d^{-1}), whose FAP is equal to 5.1×10^{-5} (Fig. 4, third panel, leftmost red dashed line). This signal has no counterpart in the periodograms of the BIS, FWHM, Crx, $\log R'_{\text{HK}}$, H α , and Na D lines. However, we found that the periodogram of the dLW shows a significant peak at 0.026 d^{-1} , corresponding to a period of about 38.4 d (green dashed line in Fig. 4). The CCF contrast shows also a peak at 0.026 d^{-1} , although

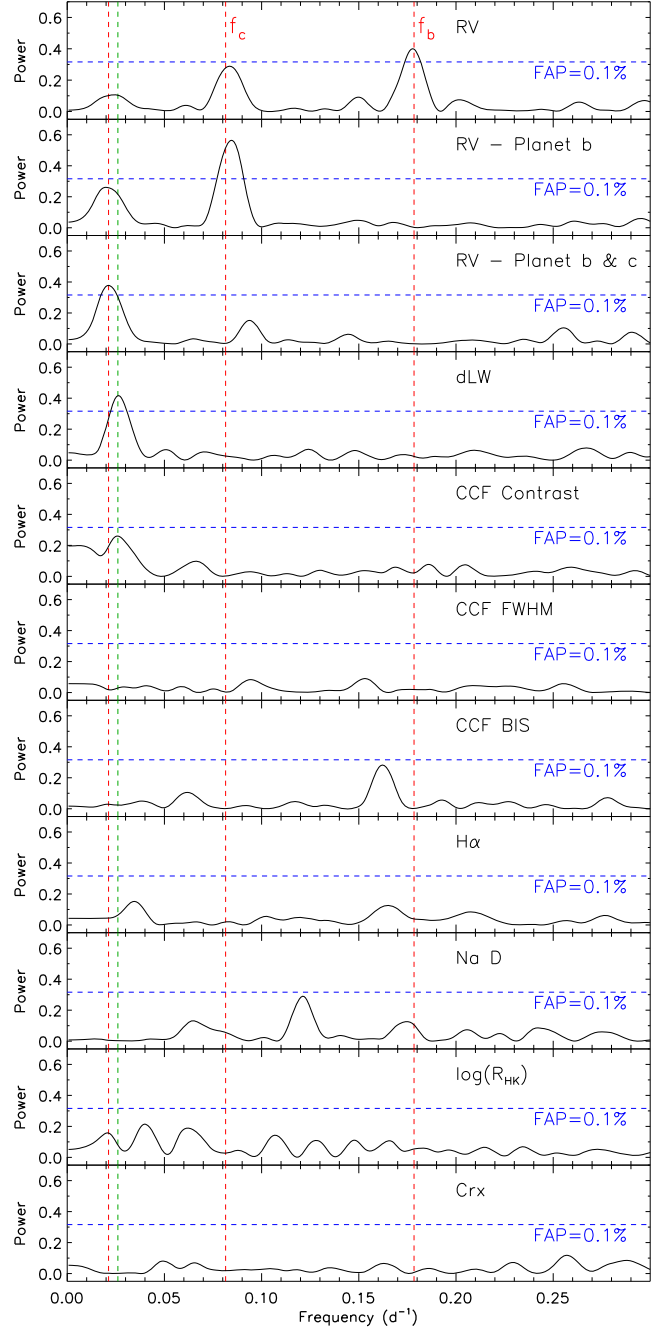


Figure 4. From the top to bottom: GLS periodogram of the HARPS RV measurements (upper panel); the RV residuals following the subtraction of the signal of TOI-763 b (second panel); the RV residuals following the subtraction of the signals of TOI-763 b and c (third panel); the dLW (fourth panel); the CCF’s contrast (fifth panel); the CCF’s FWHM (sixth panel); the CCF’s BIS (seventh panel); the H α line index (eighth panel); the Na D lines index (ninth panel); the Ca II H & K lines activity indicator (tenth panel); and the Crx index (bottom panel). The dashed vertical red lines mark the orbital frequencies of TOI-763 b and c ($f_b = 0.178$ and $f_c = 0.081 \text{ d}^{-1}$, respectively), and of the additional signal found in the HARPS RVs (0.021 d^{-1}). The dashed green line shows the frequency of the dLW peak (fourth panel from the top). The horizontal dashed blue lines mark the false alarm probability of FAP = 0.1 per cent, determined using the bootstrap randomization method described in Section 3.2.

it is not significant ($\text{FAP} \approx 0.1$ per cent). The difference between the two frequencies (0.005 d^{-1}) is about three times smaller than the spectral resolution⁴ of our RV time series (0.014 d^{-1}). This implies that the two peaks at 38.4 and 48 d remain unresolved in our data set and we cannot assess whether they arise from the same source or not. If the two peaks have a common origin, then they are likely associated with the presence of active regions carried around by stellar rotation. Alternatively, the peak at 48 d might be due the presence of an additional outer planet, whereas the peak detected in the periodogram of the dLW might be associated with magnetic activity coupled with stellar rotation.

3.3 Ground-based photometry

WASP-South, the southern station of the WASP project (Pollacco et al. 2006), consists of an array of eight cameras. From 2006 to 2012, the cameras used 200-mm, f/1.8 lenses with a filter spanning 400–700 nm. From 2012 to 2016, they used 85-mm, f/1.2 lenses with an SDSS-*r* filter (Smith & WASP Consortium 2014). On clear nights, available fields were rastered with a typical 10-min cadence. WASP-South observed the field of TOI-763 over typically 120 nights per year, accumulating 24 000 data points with the 200-mm lenses and then 43 000 datapoints with the 85-mm lenses. We searched the accumulated data on TOI-763 for a rotational modulation, using the methods presented in Maxted et al. (2011), but find no significant periodicities. For periods from 2 d up to ~ 100 d, we find an upper limit of 1 mmag for any rotational modulation.

4 HOST STAR FUNDAMENTAL PARAMETERS

4.1 Analysis of the optical spectrum

The fundamental parameters of the host star are important for deriving precise values for the planetary masses, radii, and thus bulk densities. Most important in this analysis is the effective temperature of the star, T_{eff} , and, lacking an interferometrically determined diameter of TOI-763, we derived T_{eff} from the optical HARPS data. Co-adding the 74 individual high-resolution HARPS spectra resulted in a very high S/N spectrum (about 300 per pixel at 5500 \AA). We then compared the co-added HARPS spectrum with modeled synthetic spectra. For this we used the Spectroscopy Made Easy (SME) package (Valenti & Piskunov 1996; Piskunov & Valenti 2017) version 5.22, with atomic parameters from the VALD data base (Piskunov et al. 1995). SME calculates synthetic spectra based on a number of stellar parameters using a grid of stellar atmospheric models. The grid we used in this case is based on the Atlas-12 models (Kurucz 2013). The calculated spectrum was then compared to the observed spectrum and an iterative χ^2 minimization procedure was followed until no improvement was achieved. We refer to recent papers, e.g. Persson et al. (2018) and Fridlund et al. (2017) for details about the method. In order to limit the number of free parameters, we used empirical calibrations for the V_{mic} and V_{mac} turbulence velocities (Bruntt et al. 2010; Doyle et al. 2014). The value of T_{eff} was determined from fitting the Balmer $H\alpha$ line wings. We then used the derived T_{eff} to fit a large sample of Fe I, Mg I, and Ca I lines, all with well-established atomic parameters in order to derive the abundance, $[\text{Fe}/\text{H}]$, and the $\log g$. We found the star to be slowly rotating,

⁴The spectral resolution is defined as the inverse of the baseline. For our HARPS follow-up, the baseline is ~ 73 d, which translates into a resolution of about 0.014 d^{-1} .

Table 2. Stellar parameters of the TOI-763 system.

Parameter	Unit	Star	Source
T_{eff}	(K)	5450 ± 60	4.1
$\log g$	(cgs)	4.45 ± 0.050	4.1
$[\text{Fe}/\text{H}]$	(dex)	0.01 ± 0.05	4.1
$[\text{Ca}/\text{H}]$	(dex)	0.05 ± 0.05	4.1
$[\text{Mg}/\text{H}]$	(dex)	0.12 ± 0.05	4.1
A_V	(mag)	0.02 ± 0.02	4.2
$P_{\text{rot}}/\sin i$	(d)	27 ± 16	4.4

Note. Values from spectral synthesis (SME) and the analysis of the SED.

$v \sin i_* = 1.7 \pm 0.4 \text{ km s}^{-1}$. This is consistent with the low activity as detailed in Sections 3.2 and 3.3. The star is somewhat cooler than our Sun, with an effective temperature as derived from the $H\alpha$ line wings of $T_{\text{eff}} = 5450 \pm 60$ K. Using this value for T_{eff} , we found the $[\text{Fe}/\text{H}]$ to be 0.01 ± 0.05 and the surface gravity $\log g$ to be 4.45 ± 0.05 (Table 2).

As a sanity check we also analysed the same co-added spectrum using the package SPECMATCH-EMP (Yee, Petigura & von Braun 2017). This is a public software that matches a large part of the spectrum to a library of stellar spectra with well-established fundamental parameters. We refer to Hirano et al. (2018) to describe the special procedure we used in order to match our data to the format used as input in the SPECMATCH-EMP code. The library used in this code was created, using stars that are either eclipsing binaries or that have radii determined through interferometry. We obtained a stellar radius of $R_* = 1.126 \pm 0.18 R_{\odot}$, an effective temperature of $T_{\text{eff}} = 5444 \pm 110$ K, and an iron abundance of $[\text{Fe}/\text{H}] = -0.09 \pm 0.09$. The latter two values are in agreement with the results from the SME analysis. Because of the higher precision in the SME analysis, the final adopted value of T_{eff} for TOI-763 is 5450 ± 60 K. The error is the internal errors in the synthesizing of the spectra and does not include the inherent errors of the model grid itself, as well as those errors caused by using 1D models. Finally, TOI-763 is in the *TESS*–*Gaia* catalogue of Carrillo et al. (2020), where the DR2 *Gaia* astrometry is used to compute the membership probabilities in the galactic thin disc, thick disc, and halo to be 0.954 90, 0.045 09, and 0.000 01, respectively, consistent with the solar-like metallicity derived from the spectral analysis.

4.2 Stellar radius via spectral energy distribution

We performed an analysis of the broad-band spectral energy distribution (SED) together with the *Gaia* DR2 parallax in order to determine an empirical measurement of the stellar radius, following the procedures described in Stassun & Torres (2016), Stassun, Collins & Gaudi (2017), and Stassun et al. (2018). We pulled the *BVgr* magnitudes from APASS, the *JHK_s* magnitudes from 2MASS, the *W1*–*W4* magnitudes from *WISE*, and the *G*, *G_{BP}*, and *G_{RP}* magnitudes from *Gaia* (Table 1). Together, the available photometry spans the full stellar SED over the wavelength range 0.4 – $22 \mu\text{m}$ (Fig. 5).

We performed a fit using Kurucz stellar atmosphere models, with the priors on T_{eff} , $\log g$, and $[\text{Fe}/\text{H}]$ from the spectroscopic analysis (Table 2). The remaining free parameter is the extinction (A_V), which we limited to the maximum permitted for the star’s line of sight from the Schlegel, Finkbeiner & Davis (1998) dust maps. The resulting fit is very good (Fig. 5) with a reduced χ^2 of 1.4 and $A_V = 0.02 \pm 0.02$. Integrating the model SED gives the bolometric flux at Earth of $F_{\text{bol}} = 2.345 \pm 0.055 \times 10^{-9} \text{ erg s}^{-1} \text{ cm}^{-2}$. Taking the F_{bol} and T_{eff} together with the *Gaia* parallax, adjusted by $+0.08$ mas to account

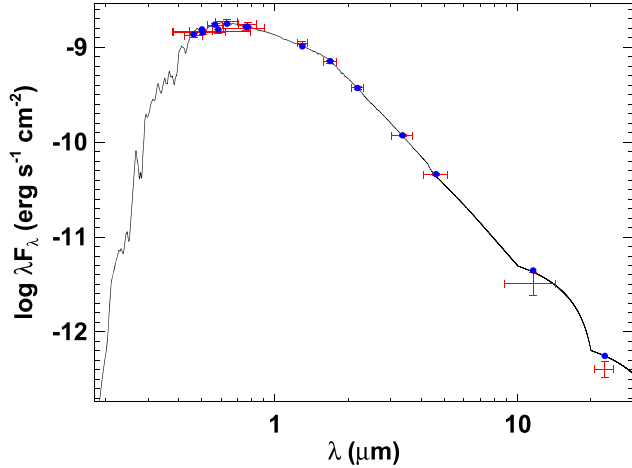


Figure 5. Spectral energy distribution. Red symbols represent the observed photometric measurements, where the horizontal bars represent the effective width of the passband. Blue symbols are the model fluxes from the best-fitting Kurucz atmosphere model (black).

Table 3. Stellar mass and radius of TOI-763 as derived from different methods.

Origin	$R_*(R_\odot)$	$M_*(M_\odot)$	Note
ExoFOP	0.9068 ± 0.047	0.97 ± 0.1146	TICv8
Specmatch	1.126 ± 0.18	-	4.1
SED	0.910 ± 0.02	0.95 ± 0.12	4.2, 4.3
Isochrones ^a	0.896 ± 0.013	0.936 ± 0.031	4.5
RV/transit	0.899 ± 0.013	0.915 ± 0.028	5.2
Num. model ^b	0.96 ± 0.031	0.96 ± 0.07	4.2, 4.3

^a Adopted for the modelling.

^b According to Torres et al. (2010).

for the systematic offset reported by Stassun & Torres (2018), gives the stellar radius as $R_* = 0.910 \pm 0.020 R_\odot$ (see Table 3).

4.3 Stellar mass via radius and surface gravity

The empirical stellar radius determined above affords an opportunity to estimate the stellar mass empirically as well, via the spectroscopically determined surface gravity ($\log g = 4.50 \pm 0.05$), which gives $M_* = 0.95 \pm 0.12 M_\odot$. This is consistent with that estimated via the eclipsing-binary-based relations of Torres, Andersen & Giménez (2010), which gives $M_* = 0.95 \pm 0.06 M_\odot$ (See Table 3).

4.4 Stellar age via activity and rotation

We used our HARPS observations to estimate the stellar age from its chromospheric activity, as measured by the Ca R'_{HK} index, which we determined to be -4.98 ± 0.03 . Using the activity–age relations of Mamajek & Hillenbrand (2008), we obtained from R'_{HK} and the star’s $B - V$ colour, an age of $\tau = 6.2 \pm 0.6$ Gyr. This is consistent with the age implied by the star’s position in the H-R diagram in comparison to the Yonsei–Yale stellar evolution models (Fig. 6).

The Mamajek & Hillenbrand (2008) relations also give a predicted rotation period for the star, based again on the R'_{HK} activity and $B - V$ colour. The derived rotation period of $P_{\text{rot}} = 32.1 \pm 1.3$ d is consistent with value inferred from the stellar radius and the spectroscopic $v \sin i_*$, which gives $P_{\text{rot}}/\sin i = 27 \pm 16$ d. Moreover, the GLS periodogram of the differential line width activity indicator

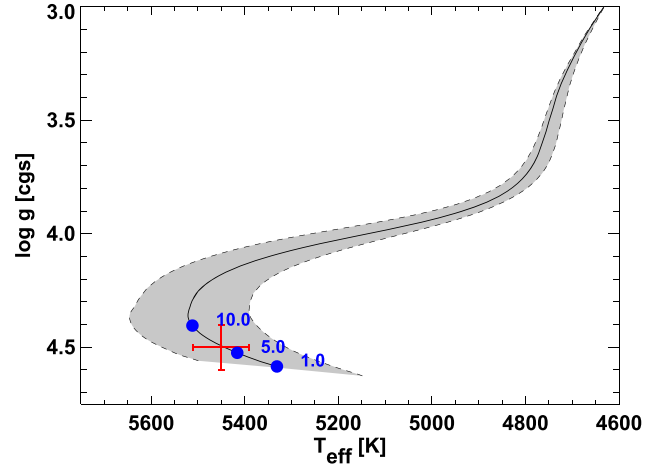


Figure 6. H-R diagram representing the observed T_{eff} and $\log g$ (red symbol) in relation to a stellar evolution model from the Yonsei–Yale grid for the star’s inferred mass and observed $[\text{Fe}/\text{H}]$; the grey swathe corresponds to the uncertainty in the inferred mass. Model ages in Gyr are represented as blue symbols.

shows a peak at ~ 38.4 d (FAP < 0.1 percent), which could be associated with stellar rotation, in agreement with the previous estimates. Altogether, all of the evidence is consistent with a slowly rotating star that is a bit older than the Sun.

4.5 Stellar parameters from isochrones

We used the PYTHON *isochrones* (Morton 2015) interface to the MIST stellar evolution models (Choi et al. 2016) to infer a uniform set of stellar parameters. We performed a fit to 2MASS *JHK* photometry (Skrutskie et al. 2006) and *Gaia* DR2 parallax (Gaia Collaboration et al. 2016, 2018) using MULTINEST (Feroz et al. 2013) to sample the joint posterior. We placed priors on T_{eff} and $[\text{Fe}/\text{H}]$ based on the spectroscopic results from SME, using a T_{eff} uncertainty of 100 K to account for systematic errors. We obtained the following parameter estimates, namely $T_{\text{eff}} = 5571 \pm 68$ K, $\log g = 4.505^{+0.022}_{-0.025}$, $[\text{Fe}/\text{H}] = 0.01 \pm 0.05$ dex, $M_* = 0.936 \pm 0.031 M_\odot$, $R_* = 0.896 \pm 0.013 R_\odot$, age = $3.8^{+2.8}_{-2.3}$ Gyr, distance = 95.48 ± 0.98 pc, and $A_V = 0.08^{+0.10}_{-0.05}$ mag, in good agreement with the values above.

5 RV AND TRANSIT ANALYSIS

5.1 Preliminary RV analysis

Using the results of our frequency analysis, we fit the HARPS RV data using *RadVel*⁵ (Fulton et al. 2018), enabling us to perform RV model selection and estimate system parameters. We tested eight different models: two circular orbits (‘2c’), two eccentric orbits (‘2e’), three circular orbits (‘3c’), three eccentric orbits (‘3e’), two circular orbits with a Gaussian Process (GP) noise model (‘2cGP’), two eccentric orbits with a GP noise model (‘2eGP’), two eccentric orbits (inner planets) and one circular orbit (outer planet), and one circular orbit (inner planet) and one eccentric orbit (outer planet). We used a quasi-periodic GP kernel (e.g. Haywood et al. 2014; Grunblatt, Howard & Haywood 2015; Dai et al. 2017) with a Gaussian prior on the period hyperparameter based on the stellar rotation period

⁵<https://github.com/California-Planet-Search/radvel>.

Table 4. RV model comparison (see Section 5.1).

Model	AICc	BIC	N_{free}	N_{data}	rms ^a	$\ln \mathcal{L}^b$
3c	315.06	336.14	11	74	1.70	−135.96
1c2e	322.28	348.56	15	74	1.62	−133.55
2e1c	323.59	349.87	15	74	1.64	−134.25
3e	327.31	355.55	17	74	1.60	−132.78
2cGP	334.28	356.81	12	74	1.69	−147.14
2c	341.21	357.43	8	74	2.15	−143.54
2eGP	342.91	370.23	16	74	1.62	−145.24
2e	346.73	369.26	12	74	2.04	−140.85

^a Root mean square of the data minus the model.^b Log-likelihood of the data, given the model.**Table 5.** MCMC posteriors from the ‘3c’ RV model (see Section 5.1).

Parameter	Cred. interval	Max. likelihood	Units
Free			
P_b	5.60501 ± 0.00094	5.605	d
T_{conj_b}	$1572.1029^{+0.0029}_{-0.003}$	1572.1029	BTJD
K_b	3.79 ± 0.31	3.79	m s^{-1}
P_c	$12.2752^{+0.004}_{-0.0038}$	12.2752	d
T_{conj_c}	$1572.9688^{+0.0032}_{-0.0031}$	1572.9687	BTJD
K_c	2.78 ± 0.31	2.77	m s^{-1}
P_d	$47.7^{+2.5}_{-1.2}$	47.7	d
T_{conj_d}	$1545.6^{+4.0}_{-7.2}$	1545.6	BTJD
K_d	$1.82^{+0.31}_{-0.32}$	1.84	m s^{-1}
γ_{HARPS}	-0.37 ± 0.21	−0.37	
σ_{HARPS}	$1.18^{+0.24}_{-0.23}$	1.06	
Derived			
$M_b \sin i$	$10.02^{+0.86}_{-0.85}$	10.37	M_{\oplus}
$M_c \sin i$	9.5 ± 1.1	9.5	M_{\oplus}
$M_d \sin i$	9.8 ± 1.7	8.1	M_{\oplus}

estimated in Section 4, $P_{\text{rot}} = 27 \pm 16$ d, and assuming zero obliquity. We present the model comparison in Table 4, including both the commonly used Bayesian information criterion (BIC) and the Akaike information criterion (AICc; corrected for small sample sizes). The ‘3c’ model (three circular orbits) is strongly favoured over the other models by both the BIC and the AIC, suggesting that eccentricity in the system is low. The MCMC parameter estimates from this model are presented in Table 5.

5.2 Joint RV and transit analysis

We jointly fit the HARPS RVs and *TESS* light curve using *exoplanet*⁶ (Foreman-Mackey, Barentsen & Barclay 2019), *starry* (Luger et al. 2019),⁷ and *pymc3*⁸ (Salvatier, Wiecki & Fonnesbeck 2016). We first used a GP model with a Matérn-3/2 kernel to fit the out-of-transit variability in the *TESS* light curve (Fig. 2). To achieve this in an accurate and efficient manner, we first masked out the transits and then binned the data by a factor of 100 (~3.3-h bins). We then conducted a joint fit to the RVs and the ‘flattened’ light curve resulting from the removal of the best-fitting GP signal, including mean flux ($\langle f \rangle$) and white

noise (σ_{TESS}) parameters for the photometry. For efficient sampling, we used quadratic limb darkening coefficients (u_1, u_2) under the transformation of Kipping (2013). We used minimally informative priors for all parameters except for the host star mass and radius, which were Gaussian and based on our results in Section 4. To reduce the possibility of underestimated uncertainties, we allowed the eccentricity of the two transiting planets to float, and included jitter (σ_{HARPS}) and mean velocity (γ_{HARPS}) parameters for the RV data.

We used the gradient-based BFGS algorithm (Nocedal & Wright 2006) implemented in *scipy.optimize* to find initial maximum a posteriori (MAP) parameter estimates. We used these estimates to initialize an exploration of parameter space via ‘no U-turn sampling’ (NUTS; Hoffman & Gelman 2014), an efficient gradient-based Hamiltonian Monte Carlo (HMC) sampler implemented in *PyMC3*. After sampling, the Gelman–Rubin statistic (Gelman & Rubin 1992) was < 1.001 and the sampling error was $\lesssim 1$ per cent for all parameters, indicating the sampler was well mixed and yielded a sufficient number of independent samples. We present the resulting parameter estimates in Table 6, and the data and posterior constraints from the model in Fig. 7. There are no significant changes in the derived semi-amplitudes of the planets from using DRS- or *serval*-extracted RVs.

As a sanity check, we also performed a joint analysis of the *TESS* and HARPS time series using *pyaneti* (Barragán, Gandolfi & Antoniciello 2019). The *pyaneti* code utilizes Bayesian approaches coupled with Markov chain Monte Carlo sampling to perform multiplanet RV and transit data fitting. We fitted the HARPS RVs using two Keplerians for the two transiting planets discovered by *TESS*, and one sine-curve for the additional Doppler signal found in the HARPS RVs. We modelled the transiting light curves using the limb-darkened quadratic model by Mandel & Agol (2002). We adopted uniform priors for all the fitted parameters but the limb-darkening coefficients, for which we used Gaussian priors based on Claret’s (2017) *TESS* coefficients. The results agree well with those previously obtained. In particular, the masses and radii agree within 1σ , or less, indicating the parameter estimates are robust.

The stellar spectroscopic parameters are consistent with a very low level of activity. We also detect no rotational modulation in either the HARPS activity indicators (Section 3.2), or in the WASP light curve (Section 3.3). Given this, we conclude that TOI-763 was about as active as our own Sun is in the quiet part of the 11-yr solar cycle at the time our observations were carried out. This is also consistent with the projected rotational velocity of $v \sin i_* = 1.7 \text{ km s}^{-1}$, thus indicating a mature G-type star (Section 4.5). Together with the indications of a rotation period of around 30 d from the $v \sin i$ and $H\alpha$ index, these circumstances make it highly unlikely that the modulation found in the HARPS Doppler time series with a period of 47.8 d (Table 6) and an RV semi-amplitude of $\sim 1.8 \text{ m s}^{-1}$ (Table 5) is caused by activity modulated by rotation.

5.3 System architecture and dynamical stability

The ratio of the orbital period of TOI-763b and TOI-763c is 2.189, which lies exterior to the 2:1 period commensurability. Planets in resonance are a sign that the planets migrated to their current observed location. Moreover, if the planets formed in the same location in a protoplanetary disc, it would be expected that they would have formed out of similar disc material and, in this manner, have comparable densities. Since the adjacent planets b and c have different densities this gives in addition hints that the planets formed

⁶<https://docs.exoplanet.codes/en/stable/>.⁷<https://rodluger.github.io/starry/v1.0.0/>.⁸<https://docs.pymc.io/>.

Table 6. DRS Joint RV and transit modelling results.

Parameter	Unit	Star			
M_*	M_\odot	0.917 ± 0.028			
R_*	R_\odot	0.897 ± 0.013			
u_1	–	0.78 ± 0.37			
u_2	–	$-0.08^{+0.43}_{-0.34}$			
$\langle f \rangle$	ppm	-17 ± 13			
σ_{TESS}	ppm	811 ± 9			
γ_{HARPS}	m s^{-1}	-0.38 ± 0.21			
σ_{HARPS}	m s^{-1}	$0.13^{+0.18}_{-0.21}$			
Parameter	Unit	Planet b	Planet c	Planet candidate d	
T_0	BTJD	1572.1020 ± 0.0031	$1572.9661^{+0.0071}_{-0.0044}$	1593.1680 ± 5.4930	
P	d	5.6057 ± 0.0013	$12.2737^{+0.0053}_{-0.0077}$	47.7991 ± 2.7399	
b	–	0.51 ± 0.35	0.51 ± 0.35	–	
e	–	$0.04^{+0.04}_{-0.03}$	$0.04^{+0.04}_{-0.03}$	$\equiv 0$	
ω	$^\circ$	42^{+57}_{-84}	62^{+78}_{-153}	$\equiv 0$	
R_P	R_*	0.023 ± 0.001	0.027 ± 0.001	–	
R_P	R_\oplus	2.28 ± 0.11	2.63 ± 0.12	–	
M_P	M_\oplus	9.79 ± 0.78	9.32 ± 1.02	9.54 ± 1.59^1	
ρ_P	g cm^{-3}	$4.51^{+0.83}_{-0.66}$	$2.82^{+0.54}_{-0.47}$	–	
a	AU	0.0600 ± 0.0006	0.1011 ± 0.0010	$0.2504^{+0.0093}_{-0.0105}$	
T_{eq}	K	1038 ± 16	800 ± 12	509 ± 12	

Note that the values for the planet candidate d are tentative.

^a $m \sin i$.

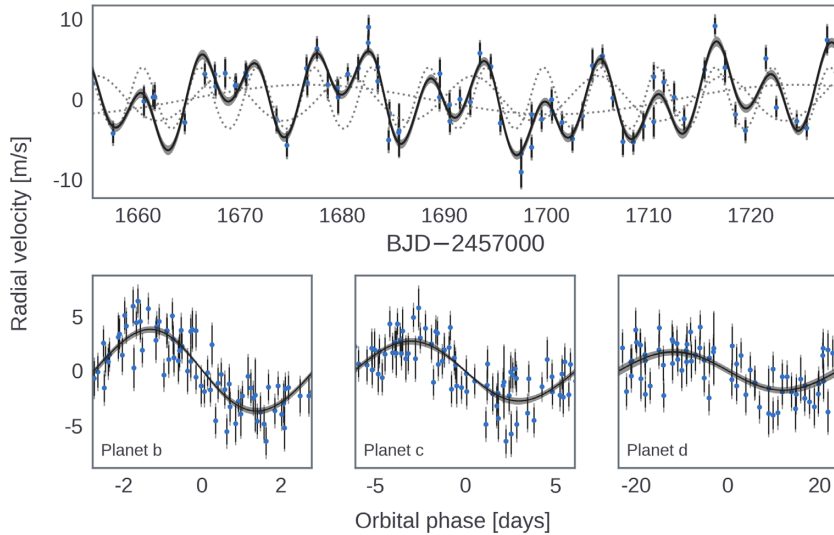


Figure 7. HARPS data (blue) and posterior constraints with 1σ credible region (black). Upper panel: full orbital solution with individual components shown as dotted lines. Lower panel: HARPS data folded on the orbital period of each planet, after subtracting the signals of the other planets. The measured error bars are in black, and the error bars taking into account the jitter (σ_{HARPS}) are in grey.

in different locations in the protoplanetary disc and migrated inwards as e.g. in the Kepler-36 systems (Carter et al. 2012).

The density of the outer serendipitously detected third planet candidate, d, close to a 4:1 period commensurability with TOI-763c, is unknown since *TESS* did not observe a transit of this planet, and we therefore measured only a lower mass limit for it. If we define a transit as an event with impact parameter ≤ 1 (that is, we ignore very grazing transits), we get 89.05° as an inclination limit for the outer planet to transit.

We carried out a set of dynamical simulations in order to study the long-term stability of the system. Here we assumed all the signals to be of planetary origin, and we wanted to investigate if any of the

parameters, in particular for the tentative planet ‘d’ could be refined. The outer planet has no upper mass constraint and only a lower mass limit derived from the RVs of $M_d \sin i = 9.54 \pm 1.59 M_\oplus$, assuming a circular orbit. We take the parameters reported in Table 6 and draw 60 000 samples from the parameters posteriors as initial parameters for the dynamical simulation. Each parameter set was integrated for 10^9 orbits of the inner planet orbital period, covering the secular interaction time-scale for the outer planet, using the Stability of the Planetary Orbital Configurations Klassifier (SPOCK; Tamayo et al. 2020). It was found that the system is dynamically stable for the whole parameter posterior space. The parameter space for the outer planet was studied in more detail whereby the true planetary mass is

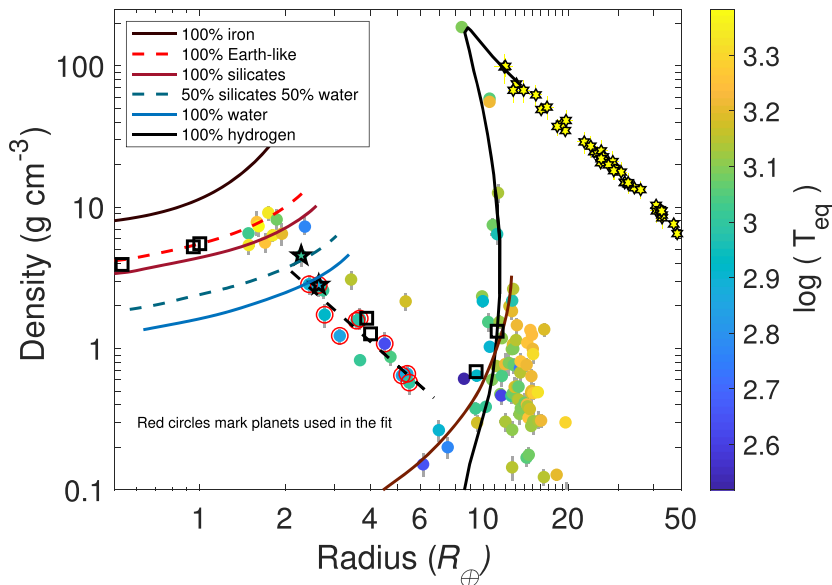


Figure 8. Density–radius diagram of planets orbiting G-type host stars with masses determined with at least 15 per cent and radii with better than 5 per cent accuracy. The two star symbols represent TOI-763b and c. The black squares are the Solar system planets, and the bright yellow star symbols at radii between 12 and 50 R_{\oplus} are red dwarf stars from Persson et al. (2018). The theoretical mass–radius curves are from Zeng et al. (2016) except the H-He model taken from Baraffe et al. (2003, 2008). The black dashed line represent a linear fit to the ice planets marked with red circles (Section 6).

drawn from the reported $m \sin i$ in Table 6 and allowing for inclination between 30° and 90° and with eccentricities up to 0.6. It is then found that stable systems can exist up to eccentricities 0.5 and for all tested inclination values. Therefore, additional observations are required to further confirm and constrain the parameters for the outer planet.

6 DISCUSSION

Data from *Kepler* have shown that G and K stars tend to have at least one planet in an orbit with a period < 100 d and that most such planets seem to be small. The most common types of planets so far tend to have masses of $\approx 2\text{--}10 M_{\oplus}$ and have radii with $R_p \approx 2\text{--}4 R_{\oplus}$ (mini-Neptunes) or with radii of $R_p \approx 1\text{--}2 R_{\oplus}$ (super-Earths), the latter thus having densities higher than those of the mini-Neptunes and potentially being rocky (Marcy et al. 2014; Petigura et al. 2017). When several planets are detected in such systems, they are often found to be in very compact arrangements where the ratio of two subsequent planet periods can often be below 2.

TOI-763 can be classified as a G-type star from its colours (Table 1). This is also confirmed by our spectral analysis in Section 4. While generally, solar-type stars are considered to be quite common, stars more massive than about G5 are rarer (Adams 2010). Taken together with the fact that our own Sun belongs to this class of stars makes the study of planet-hosting G-type objects quite worthwhile.

The planetary system accompanying TOI-763 is, however, very different from our own. It consists of two confirmed planets with masses of $M_p(b) = 9.79 M_{\oplus}$, $M_p(c) = 9.32 M_{\oplus}$, and a possible planetary candidate consistent with a minimum mass of $M_p(d)/\sin(i) = 9.54 M_{\oplus}$ in a very compact configuration, and with almost circular orbits with $a_b = 0.06$, $a_c = 0.1$, and $a_d = 0.25$ AU corresponding to orbital periods of 5.6, 12.3, and 47.8 d. The densities of the b and c planets are then 4.51 and 2.82 g cm^{-3} , respectively (Table 6). This means that even the outermost planet in the TOI-763 system would be inside the orbit of the innermost planet, Mercury, in our own planet system. The orbital period ratio of planet b and c is

2.2, which is similar to the *Kepler* compact systems, whereas the orbital period ratio of planet c and d is almost twice as high. The TOI-763 planets are also much more massive than the innermost (rocky) planets in our Solar system. With masses between 9 and 10 M_{\oplus} , they could all qualify as super-Earths with respect to mass. Being larger than twice the Earth’s radii, both planets b and c have densities that could classify them as gaseous mini-Neptunes. This demonstrates that both accurate mass and radius are crucial in order to classify planets correctly, and ultimately will improve only with asteroseismology carried out from space (García & Ballot 2019). Since planet d has only a lower mass limit, it can either be a gaseous mini-Neptune or a rocky super-Earth.

In Fig. 8, we plot a density–radius diagram of exoplanets orbiting solar-type stars, here defined as having T_{eff} between 5300 K and 6000 K. Since G stars as host stars of exoplanets tend not to be selected for dedicated studies, we choose to include only G-type stars in order to determine if they conform to the general patterns emerging in exoplanetology. To be able to determine trends in the diagram as precisely as the current data allow, and to have the same impact on density, we chose planets with a precision in mass and radius better than 15 and 5 per cent, respectively. We follow Persson et al. (2019) and Hatzes & Rauer (2015) and include transiting brown dwarfs with measured masses (cf. table 6 in Carmichael et al. 2020) in Fig. 8. We also include well-determined eclipsing M dwarfs (Persson et al. 2019), which sets the upper mass of exoplanets. The planets are colour-coded with the logarithm of the planet equilibrium temperature assuming an albedo of zero. The planet data are downloaded from the NASA exoplanet archive. We follow Otegi, Bouchy & Helled (2020) when assessing the best available measured parameters in the archive. We plot theoretical density–radius curves from iron to hydrogen (Zeng, Sasselov & Jacobsen 2016), and the H-He model from Baraffe et al. (2003), Baraffe, Chabrier & Barman (2008). The two star symbols mark the locations of TOI-763b and c. We note that the planets b and c lie

on opposite sides of the theoretical water ice line in Fig. 8, with c having the lower density. The Solar system planets (except Mercury) are also included as black squares.

As immediately visible in Fig. 8, planets fall into three separate areas of the diagram. Rocky planets can be seen in the upper left-hand side falling nicely close to the theoretical models. The ice-planets distribution follows closely a straight line from the rocky planets to the gas giants in the lower right where a turnoff is visible at a density of approximately 0.3 g cm^{-3} . The gas giants, including the brown dwarfs, follow an almost vertical branch towards higher densities with almost a constant radii. This is caused by the interior electron degeneracy pressure which increase with mass until the point when the mass is sufficient to ignite hydrogen burning, causing a sharp turnoff at densities of approximately 200 g cm^{-3} (corresponding to $75\text{--}80 M_J$). As noted in Persson et al. (2019), the gas giants with high T_{eq} have larger radii and thus lower densities than predicted by models and falls off towards the lower right-hand side.

We fit a linear polynomial to the ice planets marked with red circles located between the theoretical water and hydrogen model lines and with an equilibrium temperature of $T_{\text{eq}} < 1000 \text{ K}$. We find this polynomial to be described by $\log \rho = -1.775 \times \log(R) + 1.118$. This line would intersect the model tracks of the region between the 100 percent H and H-He models at densities of $0.2\text{--}0.3 \text{ g cm}^{-3}$ and radii of $8\text{--}10 R_{\oplus}$. This corresponds to a planet the size of Saturn, but with a density lower by more than a factor of 2 as clearly seen in Fig. 8. It is especially interesting to find that even though Uranus and Neptune, as well as TOI-763b, are excluded from the fit, they fall almost perfectly on the ‘ice-track’. This suggests that the Solar system icy planets are similar to those found outside of the Solar system as far as bulk density is concerned. What is interesting in terms of diversity is also that almost all exoplanets along the ‘ice-track’ in our figure, have orbital periods less than 23 d (one planet, Kepler-396 c, has an orbital period of 88.5 d). This is in stark contrast to Uranus and Neptune with orbital periods of 84 and 165 yr, respectively.

Having a mass roughly a factor of 1.5–2 lower than Neptune and Uranus, TOI-763b and c may have a different internal structure, since they are found on opposite sides of the water model in Fig. 8. Based on the two-layer silicate and water models of Zeng & Sasselov (2014) and the Zeng et al. (2016) models plotted in Fig. 8, we can estimate that planet b consists of a minimum of ~ 40 percent water and a maximum of ~ 60 percent silicates, while planet c has a density lower than the 100 percent water models at the corresponding location in the diagram. This is, however, neglecting the possible existence of a thick gaseous H-He atmosphere that would thus increase the radius and lower the bulk density. Both planets could then have significant rocky cores surrounded by a gaseous envelope, the diameter of which would depend on the history of energetic radiation and their respective location. These differences between planets b and c may indicate their formation in parts of the protostellar disc containing different types of material. The differences noted here would clearly benefit from the possible carrying out of transmission spectroscopy of objects like TOI-763b and c, using the *James Webb Space Telescope*/NIRISS (Doyon et al. 2012).

7 CONCLUSIONS

In this paper we have confirmed the planets, TOI-763b and c, found in the *TESS* light curves to be transiting TOI-763, and we have further been able, through extensive RV measurements, to characterize them in terms of mass and radius. We find that both TOI-763b and c should contain large amounts of water, but demonstrate significant

differences between them. We have also discovered a RV signal that could be interpreted as one additional planet, which we tentatively indicate as TOI-763d. If confirmed by later work, we have found that it should have a similar (minimum) mass as planet b and c, and an orbital period of 47.8 d. Planet d is not detected in the *TESS* photometric data.

Utilizing the high-quality data for the planetary parameters, we have compared the data for planet b and c, where we have determined high-precision bulk densities, with nine other planets with equally high precision and that are also orbiting G-type main-sequence stars. We find that these planets all belong in the density regime of ‘ice-planets’ and that their density versus radii distribution can be described by a first-degree polynomial with a very small scatter. All the planets, including TOI-763b and c, which fall along the ‘ice-track’ and orbiting stars similar to our Sun, are found in the compact arrangement with short orbital periods, similar to what has been discovered so far for smaller planets orbiting low-mass stars in general.

ACKNOWLEDGEMENTS

This work is done under the framework of the KESPRINT collaboration (<http://kesprint.science>). KESPRINT is an international consortium devoted to the characterization and research of exoplanets discovered with space-based missions. MF, CMP, and IG gratefully acknowledge the support of the Swedish National Space Agency (DNR 65/19, 174/18). This work was supported by JSPS KAKENHI Grant Number JP20K14518. This work has made use of the VALD data base, operated at Uppsala University, the Institute of Astronomy RAS in Moscow, and the University of Vienna. We are also indebted to N. Piskunov, and J. Valenti for the continued development and support of the Spectroscopy Made Easy (SME) package. This research has made use of the NASA Exoplanet Archive, which is operated by the California Institute of Technology, under contract with the National Aeronautics and Space Administration under the Exoplanet Exploration Program. This work is partly supported by JSPS KAKENHI Grant Numbers JP18H01265 and JP18H05439, and JST PRESTO Grant Number JPMJPR1775. LMS and DG gratefully acknowledge financial support from the CRT foundation under Grant No. 2018.2323 ‘Gaseous or rocky? Unveiling the nature of small worlds’. KWFL, JK, SC, ME, SG, APH, MP, and HR acknowledge support by DFG grants PA525/ 18-1, PA525/ 19-1, PA525/ 20-1, HA3279/ 12-1, and RA714/ 14-1 within the DFG Schwerpunkt SPP 1992, Exploring the Diversity of Extrasolar Planets. Resources supporting this work were provided by the NASA High-End Computing (HEC) Program through the NASA Advanced Supercomputing (NAS) Division at Ames Research Center for the production of the SPOC data products. PK and JS acknowledge the MSMT INTER-TRANSFER grant LTT20015. HD acknowledges support by grant ESP2017-87676-C5-4-R of the Spanish Secretary of State for R&D&i (MINECO). Further, we also acknowledge the comment of an anonymous referee, which improved this paper. This is University of Texas Center for Planetary Systems Habitability Contribution 0014.

8 DATA AVAILABILITY

The data underlying this study are available in this paper.

REFERENCES

- Adams F. C., 2010, *ARA&A*, 48, 47
- Baglin A., 2003, *Adv. Space Res.*, 31, 345

- Baglin A., CoRoT Team, 2016, The General Framework, The CoRoT Legacy Book: The Adventure of the Ultra High Precision Photometry from Space
- Baraffe I., Chabrier G., Barman T. S., Allard F., Hauschildt P. H., 2003, *A&A*, 402, 701
- Baraffe I., Chabrier G., Barman T., 2008, *A&A*, 482, 315
- Baranne A. et al., 1996, *A&AS*, 119, 373
- Barragán O., Gandolfi D., Antoniciello G., 2019, *MNRAS*, 482, 1017
- Borucki W. J. et al., 2010, *Science*, 327, 977
- Brunth H. et al., 2010, *A&A*, 519, A51
- Cabrera J., Csizmadia S., Erikson A., Rauer H., Kirste S., 2012, *A&A*, 548, A44
- Carmichael T. W. et al., 2020, *AJ*, 160, 53
- Carrillo A., Hawkins K., Bowler B. P., Cochran W., Vanderburg A., 2020, *MNRAS*, 491, 4365
- Carter J. A. et al., 2012, *Science*, 337, 556
- Choi J., Dotter A., Conroy C., Cantiello M., Paxton B., Johnson B. D., 2016, *ApJ*, 823, 102
- Claret A., 2017, *A&A*, 600, A30
- Dai F. et al., 2017, *AJ*, 154, 226
- Díaz M. R. et al., 2020, *MNRAS*, 493, 973
- Doyle A. P., Davies G. R., Smalley B., Chaplin W. J., Elsworth Y., 2014, *MNRAS*, 444, 3592
- Doyon R. et al., 2012, in Clampin M. C., Fazio G. G., MacEwen H. A., Oschmann J. M., Jr, eds, Proc. SPIE Conf. Ser. Vol. 8442, Space Telescopes and Instrumentation 2012: Optical, Infrared, and Millimeter Wave. SPIE, Bellingham, p. 84422R
- Feroz F., Hobson M. P., Cameron E., Pettitt A. N., 2013, *Open J. Astrophys.*, 2, 10
- Foreman-Mackey D., Barentsen G., Barclay T., 2019, dfm/exoplanet: exoplanet v0.1.5
- Fridlund M. et al., 2017, *A&A*, 604, A16
- Fulton B. J., Petigura E. A., Blunt S., Sinukoff E., 2018, *PASP*, 130, 044504
- Gaia Collaboration et al., 2016, *A&A*, 595, A1
- Gaia Collaboration et al., 2018, *A&A*, 616, A1
- García R. A., Ballot J., 2019, *Living Rev. Sol. Phys.*, 16, 4
- Gelman A., Rubin D. B., 1992, *Stat. Sci.*, 7, 457
- Grunblatt S. K., Howard A. W., Haywood R. D., 2015, *ApJ*, 808, 127
- Hatzes A. P., Rauer H., 2015, *ApJ*, 810, L25
- Haywood R. D. et al., 2014, *MNRAS*, 443, 2517
- Hippke M., Heller R., 2019, *A&A*, 623, A39
- Hirano T. et al., 2018, *AJ*, 155, 127
- Hoffman M. D., Gelman A., 2014, *J. Mach. Learn. Res.*, 15, 1593
- Howell S. B. et al., 2014, *PASP*, 126, 398
- Jenkins J. M. et al., 2016, Proc. SPIE Conf. Ser. Vol. 9913, The TESS Science Processing Operations Center, SPIE, Bellingham, p. 99133E
- Jenkins J. M., 2002, *ApJ*, 575, 493
- Kipping D. M., 2013, *MNRAS*, 435, 2152
- Kurucz R. L., 2013, Astrophysics Source Code Library, record ascl:1303.024
- Li J., Tenenbaum P., Twicken J. D., Burke C. J., Jenkins J. M., Quintana E. V., Rowe J. F., Seader S. E., 2019, *PASP*, 131, 024506
- Lovis C., Pepe F., 2007, *A&A*, 468, 1115
- Luger R., Agol E., Foreman-Mackey D., Fleming D. P., Lustig-Yaeger J., Deitrick R., 2019, *AJ*, 157, 64
- Malavolta L. et al., 2017, *AJ*, 153, 224
- Mamajek E. E., Hillenbrand L. A., 2008, *ApJ*, 687, 1264
- Mandel K., Agol E., 2002, *ApJ*, 580, L171
- Marcy G. W., Weiss L. M., Petigura E. A., Isaacson H., Howard A. W., Buchhave L. A., 2014, *Proc. Natl. Acad. Sci.*, 111, 12655
- Maxted P. F. L. et al., 2011, *PASP*, 123, 547
- Mayor M. et al., 2003, The Messenger, 114, 20
- Mayor M., Queloz D., 1995, *Nature*, 378, 355
- Morton T. D., 2015, Astrophysics Source Code Library, record ascl:1503.010
- Murdoch K. A., Hearnshaw J. B., Clark M., 1993, *ApJ*, 413, 349
- Nielsen L. D. et al., 2020, *MNRAS*, 492, 5399
- Nocedal J., Wright S. J., 2006, Numerical Optimization, 2nd edn. Springer, New York, NY
- Otegi J. F., Bouchy F., Helled R., 2020, *A&A*, 634, A43
- Pepe F., Mayor M., Galland F., Naef D., Queloz D., Santos N. C., Udry S., Burnet M., 2002, *A&A*, 388, 632
- Persson C. M. et al., 2018, *A&A*, 618, A33
- Persson C. M. et al., 2019, *A&A*, 628, A64
- Petigura E. A. et al., 2017, *AJ*, 153, 142
- Piskunov N., Valenti J. A., 2017, *A&A*, 597, A16
- Piskunov N. E., Kupka F., Ryabchikova T. A., Weiss W. W., Jeffery C. S., 1995, *A&AS*, 112, 525
- Pollacco D. L. et al., 2006, *PASP*, 118, 1407
- Press W. H., Teukolsky S. A., Vetterling W. T., Flannery B. P., 2002, Numerical Recipes in C++: The Art of Scientific Computing, <https://ui.adsabs.harvard.edu/abs/2002nrca.book.....P>
- Rauer H. et al., 2014, *Exp. Astron.*, 38, 249
- Ricker G. R. et al., 2015, *J. Astron. Telesc. Instrum. Syst.*, 1, 014003
- Salvatier J., Wiecki T. V., Fonnesbeck C., 2016, *PeerJ Comput. Sci.*, 2, e55
- Savitzky A., Golay M. J. E., 1964, *Anal. Chem.*, 36, 1627
- Schlegel D. J., Finkbeiner D. P., Davis M., 1998, *ApJ*, 500, 525
- Skrutskie M. F. et al., 2006, *AJ*, 131, 1163
- Smith J. C. et al., 2012, *PASP*, 124, 1000
- Smith A. M. S., WASP Consortium, 2014, *Contrib. Astron. Obs. Skalnaté Pleso*, 43, 500
- Stassun K. G. et al., 2018, *AJ*, 156, 102
- Stassun K. G., Torres G., 2016, *ApJ*, 831, L6
- Stassun K. G., Torres G., 2018, *ApJ*, 862, 61
- Stassun K. G., Collins K. A., Gaudi B. S., 2017, *AJ*, 153, 136
- Stumpe M. C. et al., 2012, *PASP*, 124, 985
- Tamayo D. et al., 2020, preprint ([arXiv:2007.0652](https://arxiv.org/abs/2007.0652))
- Torres G., Andersen J., Giménez A., 2010, *A&AR*, 18, 67
- Twicken J. D. et al., 2018, *PASP*, 130, 064502
- Valenti J. A., Piskunov N., 1996, *A&AS*, 118, 595
- Yee S. W., Petigura E. A., von Braun K., 2017, *ApJ*, 836, 77
- Zechmeister M. et al., 2018, *A&A*, 609, A12
- Zechmeister M., Kürster M., 2009, *A&A*, 496, 577
- Zeng L., Sasselov D., 2014, *ApJ*, 784, 96
- Zeng L., Sasselov D. D., Jacobsen S. B., 2016, *ApJ*, 819, 127

APPENDIX A: THE RV DATA

Table A1. TOI-763's HARPS RVs, CCF's bisector inverse slope (BIS), CCF's full width at half-maximum (FWHM), CCF's contrast, and Ca II H&K line activity indicator ($\log R'_{\text{HK}}$) as extracted using the HARPS data reduction software (dhrs).

BJD _{TDB} −2450000 (d)	RV (km s ^{−1})	σ_{RV} (km s ^{−1})	BIS (km s ^{−1})	FWHM (km s ^{−1})	Contrast	$\log R'_{\text{HK}}$	$\sigma_{\log R'_{\text{HK}}}$	T_{exp} (s)	S/N per pixel @5550 Å
8655.574286	−13.9795	0.0019	−0.0277	6.8118	49.046	−5.005	0.025	1800	47.5
8657.585518	−13.9857	0.0012	−0.0216	6.8193	48.978	−4.964	0.014	1800	74.5
8660.605351	−13.9818	0.0018	−0.0288	6.8142	49.065	−5.020	0.030	1800	52.8
8661.499253	−13.9813	0.0012	−0.0322	6.8216	49.053	−4.958	0.014	1800	73.8
8661.631697	−13.9812	0.0015	−0.0293	6.8157	49.056	−5.048	0.028	1800	63.5
8664.593171	−13.9844	0.0011	−0.0228	6.8287	49.027	−4.960	0.015	1800	85.4
8666.546629	−13.9784	0.0013	−0.0310	6.8271	49.038	−4.976	0.018	1800	70.0
8667.533554	−13.9784	0.0012	−0.0252	6.8165	49.039	−4.955	0.017	1800	76.9
8667.608594	−13.9799	0.0011	−0.0252	6.8171	49.056	−4.966	0.016	1800	81.0
8668.562153	−13.9783	0.0017	−0.0231	6.8288	48.991	−4.965	0.023	1800	52.7
8669.518396	−13.9798	0.0011	−0.0212	6.8221	48.966	−4.920	0.009	1800	78.3
8669.594177	−13.9798	0.0011	−0.0288	6.8187	48.947	−4.934	0.011	1800	81.7
8670.536138	−13.9782	0.0012	−0.0267	6.8167	49.020	−4.951	0.015	1800	76.5
8670.606619	−13.9786	0.0013	−0.0319	6.8250	48.997	−4.982	0.017	1800	72.0
8673.578403	−13.9841	0.0014	−0.0268	6.8163	48.964	−4.998	0.020	1800	64.9
8674.584085	−13.9872	0.0014	−0.0249	6.8324	48.908	−4.989	0.021	1800	65.9
8676.495617	−13.9777	0.0014	−0.0261	6.8243	48.996	−4.984	0.020	1800	66.3
8676.567243	−13.9795	0.0015	−0.0356	6.8266	48.967	−4.985	0.025	1800	62.7
8677.509955	−13.9752	0.0012	−0.0314	6.8231	49.009	−5.037	0.020	1800	75.0
8678.584762	−13.9797	0.0016	−0.0351	6.8174	49.041	−5.018	0.030	1800	59.4
8679.531662	−13.9801	0.0010	−0.0285	6.8210	49.006	−5.005	0.015	1800	91.0
8679.596749	−13.9812	0.0020	−0.0403	6.8162	49.030	−5.072	0.055	1800	50.8
8680.539773	−13.9784	0.0008	−0.0282	6.8238	49.016	−4.981	0.011	1800	108.4
8681.547466	−13.9777	0.0014	−0.0257	6.8198	49.005	−5.029	0.024	1800	66.0
8682.528206	−13.9745	0.0010	−0.0263	6.8223	49.020	−4.982	0.013	1800	86.5
8682.576813	−13.9726	0.0011	−0.0238	6.8221	49.004	−4.983	0.016	1800	80.2
8683.470732	−13.9776	0.0013	−0.0306	6.8303	48.968	−4.981	0.017	1800	70.5
8683.490255	−13.9793	0.0013	−0.0309	6.8131	49.034	−4.957	0.016	1800	69.1
8684.558927	−13.9866	0.0012	−0.0280	6.8276	48.949	−4.972	0.015	1800	73.7
8684.621364	−13.9833	0.0014	−0.0340	6.8268	48.995	−5.020	0.024	1800	67.7
8685.519032	−13.9856	0.0012	−0.0276	6.8247	49.023	−4.983	0.018	1800	76.4
8685.565024	−13.9854	0.0033	−0.0305	6.8062	49.075	−5.141	0.114	1800	34.2
8689.528163	−13.9813	0.0015	−0.0230	6.8234	49.019	−4.978	0.022	1800	64.0
8689.572326	−13.9783	0.0017	−0.0301	6.8198	49.038	−5.053	0.036	1800	55.6
8690.507814	−13.9822	0.0015	−0.0319	6.8228	49.016	−5.009	0.022	1800	60.5
8690.532153	−13.9843	0.0013	−0.0278	6.8234	49.061	−4.958	0.017	1800	67.0
8691.510994	−13.9815	0.0012	−0.0298	6.8184	49.040	−5.001	0.018	2100	76.5
8692.539322	−13.9819	0.0016	−0.0299	6.8223	49.070	−5.013	0.024	1800	57.9
8693.488271	−13.9758	0.0013	−0.0309	6.8227	49.064	−4.991	0.018	1800	71.7
8694.515083	−13.9774	0.0012	−0.0274	6.8182	49.047	−4.977	0.016	1500	74.7
8694.532628	−13.9775	0.0012	−0.0240	6.8225	49.040	−4.986	0.016	1500	79.9
8695.485141	−13.9845	0.0011	−0.0304	6.8261	49.033	−4.963	0.013	1800	84.0
8697.505285	−13.9883	0.0018	−0.0292	6.8194	49.012	−4.967	0.029	1800	53.7
8697.526684	−13.9906	0.0019	−0.0298	6.8219	49.028	−5.043	0.038	1800	51.6
8698.514889	−13.9834	0.0012	−0.0290	6.8191	49.020	−4.967	0.016	1800	73.4
8698.534830	−13.9875	0.0013	−0.0271	6.8231	49.023	−4.942	0.016	1800	72.8
8699.502250	−13.9840	0.0012	−0.0251	6.8228	49.024	−4.978	0.017	1800	79.1
8700.490814	−13.9815	0.0012	−0.0245	6.8143	49.002	−4.999	0.017	1800	76.6
8700.511796	−13.9830	0.0012	−0.0196	6.8163	49.002	−4.954	0.015	1800	79.5
8701.515464	−13.9844	0.0011	−0.0290	6.8184	48.995	−4.962	0.015	1800	89.4
8702.518461	−13.9864	0.0014	−0.0270	6.8170	48.974	−5.002	0.024	1800	66.4
8703.523842	−13.9836	0.0015	−0.0332	6.8290	48.929	−4.988	0.025	2100	61.9
8704.499781	−13.9773	0.0020	−0.0286	6.8309	48.910	−5.029	0.038	2400	49.3
8705.474923	−13.9761	0.0010	−0.0282	6.8175	49.008	−4.991	0.014	1800	93.7
8706.476486	−13.9814	0.0011	−0.0266	6.8184	48.972	−4.965	0.015	1800	82.4
8707.484588	−13.9868	0.0017	−0.0295	6.8184	48.944	−4.996	0.026	2400	56.5
8708.490874	−13.9869	0.0012	−0.0341	6.8251	48.960	−4.986	0.017	1800	77.7
8709.483806	−13.9848	0.0016	−0.0306	6.8147	49.000	−4.975	0.026	1800	60.8
8710.481089	−13.9787	0.0015	−0.0305	6.8206	49.023	−5.008	0.024	1800	63.8
8710.499999	−13.9843	0.0018	−0.0287	6.8191	48.971	−5.023	0.034	1800	53.5
8711.475294	−13.9794	0.0013	−0.0270	6.8222	48.954	−4.979	0.018	2100	75.0

Table A1 – continued

BJD _{TDB} –2450000 (d)	RV (km s ^{–1})	σ_{RV} (km s ^{–1})	BIS (km s ^{–1})	FWHM (km s ^{–1})	Contrast	$\log R'_{HK}$	$\sigma_{\log R'_{HK}}$	T_{exp} (s)	S/N per pixel @5550 Å
8712.492704	–13.9813	0.0018	–0.0269	6.8286	48.936	–5.004	0.030	2100	54.6
8713.481667	–13.9840	0.0014	–0.0276	6.8160	48.985	–4.956	0.019	2100	68.0
8715.477396	–13.9778	0.0012	–0.0292	6.8233	48.968	–4.945	0.014	2400	79.3
8716.475018	–13.9724	0.0010	–0.0271	6.8255	48.960	–4.933	0.012	1800	92.8
8717.475742	–13.9776	0.0018	–0.0282	6.8276	48.908	–4.968	0.028	1800	52.0
8718.474720	–13.9834	0.0012	–0.0229	6.8220	48.959	–4.933	0.015	1800	77.1
8719.476638	–13.9854	0.0013	–0.0261	6.8197	48.954	–5.006	0.021	1800	74.3
8721.475163	–13.9764	0.0013	–0.0260	6.8147	48.967	–4.968	0.020	1800	72.0
8722.480011	–13.9826	0.0011	–0.0296	6.8186	49.002	–4.976	0.017	1800	84.1
8724.475162	–13.9843	0.0009	–0.0288	6.8192	48.988	–4.957	0.010	1800	100.6
8725.476170	–13.9851	0.0011	–0.0250	6.8168	49.007	–4.970	0.016	1800	86.9
8727.475528	–13.9741	0.0017	–0.0340	6.8129	48.956	–5.097	0.036	1800	58.6
8728.477649	–13.9758	0.0015	–0.0330	6.8221	48.960	–5.013	0.025	2100	62.3

Note. The exposure time and S/N per pixel at 5500 Å are listed in the last two columns.

Table A2. TOI-763's HARPS differential line width (dLW), chromatic index (Crx), and Na D and H α line activity indicators extracted with the spectrum RV analyser (*serval*).

BJD _{TDB} –2450000 (d)	dLW (m ² s ^{–2})	σ_{dLW} (m ² s ^{–2})	Crx (m s ^{–1} Np ^{–1})	σ_{Crx} (m s ^{–1} Np ^{–1})	H α	$\sigma_{H\alpha}$	Na D	σ_{NaD}
8655.574286	–27.3234	3.4815	–13.6056	13.3345	0.4439	0.0018	0.2781	0.0021
8657.585518	–34.9508	2.2257	–9.8812	11.1881	0.4416	0.0011	0.2719	0.0012
8660.605351	–34.1636	3.0802	–13.6919	13.9300	0.4436	0.0016	0.2781	0.0018
8661.499253	–30.3810	2.4287	–4.0789	10.7817	0.4395	0.0011	0.2774	0.0012
8661.631697	–32.4117	2.7012	17.6440	14.2956	0.4429	0.0013	0.2735	0.0014
8664.593171	–30.4048	1.9665	–10.5227	8.8589	0.4398	0.0009	0.2799	0.0011
8666.546629	–29.9505	1.9517	11.0804	11.7434	0.4410	0.0012	0.2726	0.0013
8667.533554	–30.8120	2.2702	8.4083	11.1142	0.4408	0.0010	0.2761	0.0012
8667.608594	–33.0404	2.3743	1.7582	10.8517	0.4383	0.0010	0.2727	0.0011
8668.562153	–27.1619	3.3684	–2.5544	14.7873	0.4438	0.0016	0.2765	0.0018
8669.518396	–19.2356	2.1273	–3.4056	10.8156	0.4423	0.0011	0.2752	0.0012
8669.594177	–19.1052	2.0280	–3.7332	11.8615	0.4406	0.0010	0.2813	0.0011
8670.536138	–29.0092	2.2689	–2.7832	10.5860	0.4414	0.0010	0.2801	0.0012
8670.606619	–24.9930	2.1656	–0.1078	12.1134	0.4394	0.0011	0.2785	0.0013
8673.578403	–26.6192	2.3838	2.4626	12.9057	0.4382	0.0013	0.2756	0.0014
8674.584085	–24.7986	2.9662	6.7085	11.4400	0.4401	0.0012	0.2717	0.0014
8676.495617	–28.5964	2.6941	–12.1365	11.3112	0.4375	0.0012	0.2715	0.0014
8676.567243	–26.4019	3.5562	–8.3655	13.7688	0.4384	0.0013	0.2728	0.0015
8677.509955	–22.6246	2.7620	–5.5261	9.9081	0.4424	0.0011	0.2747	0.0012
8678.584762	–17.4065	3.2822	0.0232	13.4401	0.4430	0.0013	0.2810	0.0016
8679.531662	–29.2413	2.3215	–4.0168	9.9460	0.4418	0.0009	0.2770	0.0010
8679.596749	–15.9057	4.5005	33.3329	16.8297	0.4435	0.0015	0.2836	0.0018
8680.539773	–26.7658	1.9028	–10.6048	9.3233	0.4404	0.0007	0.2767	0.0008
8681.547466	–18.2137	3.4352	7.4320	11.0308	0.4402	0.0012	0.2787	0.0014
8682.528206	–24.8256	2.1641	–0.9159	7.0255	0.4388	0.0009	0.2775	0.0010
8682.576813	–28.1810	2.1110	1.8850	10.6389	0.4392	0.0010	0.2767	0.0011
8683.470732	–25.2732	2.7230	–4.5382	11.2486	0.4413	0.0011	0.2799	0.0013
8683.490255	–28.7430	2.5488	–2.2769	13.2397	0.4414	0.0012	0.2791	0.0013
8684.558927	–24.7389	2.5555	–5.2513	11.5722	0.4427	0.0011	0.2731	0.0012
8684.621364	–24.3193	3.1360	–0.9628	10.2176	0.4422	0.0012	0.2702	0.0013
8685.519032	–29.4160	2.6435	8.1137	9.9926	0.4414	0.0010	0.2791	0.0012
8685.565024	–32.8843	6.6776	26.1068	25.8119	0.4436	0.0024	0.2793	0.0029
8689.528163	–27.6250	2.3541	3.5240	16.1837	0.4412	0.0012	0.2746	0.0014
8689.572326	–32.6538	3.2969	–3.0382	20.6879	0.4400	0.0014	0.2744	0.0017
8690.507814	–31.3709	2.8905	5.1231	13.7563	0.4423	0.0014	0.2755	0.0016
8690.532153	–32.3343	2.8776	8.9537	12.6298	0.4417	0.0012	0.2734	0.0014
8691.510994	–33.8941	2.6392	–12.2249	10.9119	0.4389	0.0010	0.2710	0.0012
8692.539322	–34.7286	3.1755	7.5525	12.9709	0.4382	0.0014	0.2763	0.0016
8693.488271	–32.6269	2.6853	10.5369	12.3633	0.4394	0.0011	0.2765	0.0013
8694.515083	–30.1416	2.7134	2.8462	9.0025	0.4388	0.0011	0.2784	0.0012
8694.532628	–29.5008	2.4497	0.0987	9.5962	0.4415	0.0010	0.2784	0.0011

Table A2 – *continued*

BJD _{TDB} –2450000 (d)	dLW (m ² s ^{–2})	σ_{dLW} (m ² s ^{–2})	CrX (m s ^{–1} Np ^{–1})	σ_{CrX} (m s ^{–1} Np ^{–1})	H α	$\sigma_{\text{H}\alpha}$	Na D	σ_{NaD}
8695.485141	–30.2703	2.2118	–2.0782	9.6373	0.4397	0.0010	0.2769	0.0011
8697.505285	–32.9234	3.7203	19.9173	11.3887	0.4393	0.0015	0.2829	0.0017
8697.526684	–32.4152	3.7858	14.7366	13.3673	0.4397	0.0015	0.2817	0.0018
8698.514889	–32.5441	2.5370	–5.6555	10.0501	0.4411	0.0011	0.2801	0.0012
8698.534830	–31.2862	2.6793	–0.8187	9.5557	0.4404	0.0011	0.2786	0.0012
8699.502250	–31.5803	2.3837	–7.1028	10.2506	0.4383	0.0010	0.2738	0.0011
8700.490814	–30.0590	2.4068	0.5601	9.8587	0.4404	0.0010	0.2729	0.0012
8700.511796	–32.0105	2.0274	9.6646	9.7858	0.4382	0.0010	0.2745	0.0011
8701.515464	–32.4156	2.0589	0.2134	7.9769	0.4405	0.0008	0.2706	0.0010
8702.518461	–32.8061	2.8615	–19.3266	12.4775	0.4389	0.0012	0.2723	0.0014
8703.523842	–26.9803	3.0420	–6.9396	13.1684	0.4396	0.0013	0.2718	0.0015
8704.499781	–24.2002	4.3921	3.4798	17.7909	0.4395	0.0016	0.2860	0.0019
8705.474923	–28.2223	1.7840	–1.9189	7.7832	0.4402	0.0008	0.2776	0.0010
8706.476486	–29.3501	2.2899	5.5727	8.8095	0.4388	0.0009	0.2710	0.0011
8707.484588	–15.5731	3.1948	–1.2679	14.0285	0.4388	0.0014	0.2744	0.0016
8708.490874	–23.6189	2.7607	1.1063	9.5419	0.4418	0.0010	0.2710	0.0012
8709.483806	–14.6217	3.6523	14.3927	12.0294	0.4420	0.0013	0.2736	0.0015
8710.481089	–23.0342	3.2025	29.8668	13.5686	0.4396	0.0012	0.2806	0.0014
8710.499999	–7.3168	4.7679	44.4273	13.5357	0.4399	0.0015	0.2775	0.0017
8711.475294	–16.1286	3.1201	–4.7268	11.7724	0.4403	0.0010	0.2843	0.0012
8712.492704	–18.6837	3.4692	–1.9183	14.8572	0.4413	0.0014	0.2772	0.0017
8713.481667	–27.0469	2.8001	–5.2989	11.5990	0.4411	0.0012	0.2762	0.0014
8715.477396	–22.7484	2.3661	–6.6190	10.1799	0.4419	0.0010	0.2795	0.0011
8716.475018	–25.0995	2.1692	2.4860	9.2656	0.4423	0.0008	0.2714	0.0010
8717.475742	–21.9609	3.8755	–1.4322	17.3181	0.4410	0.0015	0.2744	0.0018
8718.474720	–23.7491	2.3748	3.2041	11.6205	0.4408	0.0010	0.2727	0.0012
8719.476638	–29.0434	2.8562	–10.6933	12.1987	0.4420	0.0010	0.2795	0.0012
8721.475163	–27.9779	2.6364	2.3398	11.0052	0.4414	0.0011	0.2722	0.0012
8722.480011	–27.7482	2.3911	–8.0116	10.3813	0.4399	0.0009	0.2801	0.0011
8724.475162	–26.6539	2.1566	1.0507	7.3636	0.4401	0.0008	0.2721	0.0009
8725.476170	–25.7527	2.2573	5.1373	8.0819	0.4395	0.0009	0.2730	0.0010
8727.475528	–18.7502	3.8639	24.3561	14.6378	0.4404	0.0013	0.2798	0.0016
8728.477649	–24.0673	3.1167	20.2222	12.1625	0.4415	0.0013	0.2803	0.0015

¹Leiden Observatory, Leiden University, NL-2333 CA Leiden, The Netherlands²Department of Space, Earth and Environment, Chalmers University of Technology, Onsala Space Observatory, SE-439 92 Onsala, Sweden³Department of Astronomy, University of Tokyo, 7-3-1 Hongo, Bunkyo-ky, Tokyo 113-0033, Japan⁴Dipartimento di Fisica, Università degli Studi di Torino, via Pietro Giuria 1, I-10125 Torino, Italy⁵Center for Astronomy and Astrophysics, Technical University Berlin, Hardenbergstr. 36, D-10623 Berlin, Germany⁶Physics and Astronomy Department, Vanderbilt University, Nashville, TN 37235, USA⁷Astrophysics Group, Keele University, Staffordshire ST5 5BG, UK⁸Rheinisches Institut für Umweltforschung an der Universität zu Köln, Aachener Strasse 209, D-50931 Köln, Germany⁹Thüringer Landessternwarte Tautenburg, D-07778 Tautenburg, Germany¹⁰Dipartimento di Fisica e Astronomia Galilei, Università di Padova, Vicolo dell'Osservatorio 3, I-35122 Padova, Italy¹¹Instituto de Astrofísica de Canarias, C/Vía Lactea s/n, E-38205 La Laguna, Spain¹²Departamento de Astrofísica, Universidad de La Laguna, E-38206 La Laguna, Spain¹³Astronomy Department and Van Vleck Observatory, Wesleyan University, Middletown, CT 06459, USA¹⁴Stellar Astrophysics Centre, Department of Physics and Astronomy, Aarhus University, Ny Munkegade 120, DK-8000 Aarhus C, Denmark¹⁵Sub-department of Astrophysics, Department of Physics, University of Oxford, Oxford OX1 3RH, UK¹⁶INAF – Osservatorio Astronomico di Palermo, Piazza del Parlamento, 1, I-90134 Palermo, Italy¹⁷Department of Astrophysical Sciences, Princeton University, 4 Ivy Lane, Princeton, NJ 08544, USA¹⁸Institute of Planetary Research, German Aerospace Center, Rutherfordstrasse 2, D-12489 Berlin, Germany¹⁹Department of Astronomy and McDonald Observatory, University of Texas at Austin, 2515 Speedway, Stop C1400, Austin, TX 78712, USA²⁰Center for Planetary Systems Habitability, University of Texas at Austin, Austin, TX 78712, USA²¹Department of Physics and Kavli Institute for Astrophysics and Space Research, Massachusetts Institute of Technology, Cambridge, MA 02139, USA²²Department of Earth and Planetary Sciences, Tokyo Institute of Technology, 2-12-1 Ookayama, Meguro-ku, Tokio 152-8551, Japan²³NASA Ames Research Center, Moffet Field, CA 94035, USA²⁴Astronomical Institute, Czech Academy of Sciences, Fričova 298, CZ-25165 Ondřejov, Czech Republic²⁵Center for Astrophysics | Harvard & Smithsonian, 60 Garden Street, Cambridge, MA 02138, USA²⁶Department of Aeronautics and Astronautics, MIT, 77 Massachusetts Avenue, Cambridge, MA 02139, USA²⁷National Astronomical Observatory of Japan, NINS, 2-21-1 Osawa, Mitaka, Tokyo 1818588, Japan²⁸Komaba Institute for Science, The University of Tokyo, 3-8-1 Komaba, Meguro, Tokyo 153-8902, Japan²⁹JST, PRESTO, 3-8-1 Komaba, Meguro, Tokyo 153-8902, Japan³⁰Astrobiology Center, NINS, 2-21-1 Osawa, Mitaka, Tokyo 181-8588, Japan

³¹*European Southern Observatory (ESO), Alonso de Córdova 3107, Vitacura, Casilla 19001, Santiago de Chile, Chile*

³²*Institut fuer Geologische Wissenschaften, Freie Universitaet Berlin, D-12249 Berlin, Germany*

³³*Department of Earth, Atmospheric and Planetary Sciences, Massachusetts Institute of Technology, Cambridge, MA 02139, USA*

³⁴*School of Physics and Astronomy, Monash University, VIC 3800, Australia*

³⁵*ARC Centre of Excellence for All Sky Astrophysics in Three Dimensions (ASTRO-3D), Canberra, ACT 2601, Australia*

³⁶*Astronomical Institute, Faculty of Mathematics and Physics, Charles University, Ke Karlovu 2027/3, CZ-12116 Prague, Czech Republic*

³⁷*SETI Institute/NASA Ames Research Center, Moffet Field, CA 94035, USA*

³⁸*Department of Astronomy, University of Wisconsin-Madison, Madison, WI 53706, USA*

³⁹*Mullard Space Science Laboratory, University College London, Holmbury St Mary, Dorking, Surrey RH5 6NT, UK*

This paper has been typeset from a \LaTeX file prepared by the author.